Integrating high-precision aftershock locations and geodetic observations to model coseismic deformation associated with the 1995 Kozani-Grevena earthquake, Greece

P. G. Resor[1] and D. D. Pollard
Department of Geological and Environmental Sciences, Stanford University, Stanford, California, USA

T. J. Wright
COMET, Department of Earth Sciences, University of Oxford, Oxford, UK

G. C. Beroza
Department of Geophysics, Stanford University, Stanford, California, USA

Received 26 June 2004; revised 7 April 2005; accepted 25 May 2005; published 2 September 2005.

[1] We integrate high-precision aftershock locations with geodetic inverse modeling to create a more complete kinematic model for the Kozani-Grevena earthquake sequence. Using the double-difference algorithm, we have improved relative hypocentral locations by a factor of ~7 and thus imaged the details of the fault network associated with the seismic sequence. The interpreted fault network consists of multiple segments including (1) a master normal fault that strikes nearly due west and dips toward the north at 43°, extending from 6 to 15 km depth; (2) an upper segment that connects the top of the seismicity to the observed surface ruptures and dips 70°; (3) hanging wall antithetic faults; (4) a more steeply dipping southwest striking linking structure at the southwest end of the rupture; and (5) a separate south dipping segment at the southwestern end of the aftershock cluster. The imaged fault segment dimensions, orientations, and geometric relationships are consistent with regional fault patterns. Using slip inversion on triangular dislocation patches, we calculate variable slip on the imaged three-dimensional fault network that best fits the surface displacements observed by satellite interferometric synthetic aperture radar (InSAR). In our preferred model we find that the majority of slip occurred at depth on the west and southwest striking segments. By comparing these results to a planar fault model derived solely from the InSAR data using nonlinear inversion methods we demonstrate that the three-dimensional model improves the fit to the geodetic data while incorporating the observations of surface rupturing and aftershock distributions.

Citation: Resor, P. G., D. D. Pollard, T. J. Wright, and G. C. Beroza (2005), Integrating high-precision aftershock locations and geodetic observations to model coseismic deformation associated with the 1995 Kozani-Grevena earthquake, Greece, *J. Geophys. Res.*, *110*, B09402, doi:10.1029/2004JB003263.

1. Introduction

[2] A number of recent damaging normal fault earthquakes have been associated with little or no surface rupture (e.g., M_w 6.0 Athens, Greece, 1999; M_w 5–6 Colfiorito sequence (Umbria-Marche), Italy, 1997; M_w 6.5 Kozani-Grevena, Greece, 1995). The lack of significant surface rupture and the complex pattern of nearby faults have led to debate about which faults caused the events and the three-dimensional geometry of these faults. A better understanding of the fault geometry associated with these earthquakes is important for assessing local seismic hazard as well as gaining a better understanding of the role that fault geometry plays in the earthquake rupture process. Fault bends and discontinuities act as local stress concentrators [e.g., *Segall and Pollard*, 1987], and it has been proposed that they may play important roles in earthquake nucleation and arrest [e.g., *King*, 1986; *Schwartz and Coppersmith*, 1984]. In addition, the downdip geometry of normal faults (i.e., are they curved (listric) or planar?) has been a long-standing point of contention [*Jackson and White*, 1989; *Stein and Barrientos*, 1985; *Wernicke et al.*, 1992]. In this paper we revisit the 1995 Kozani-Grevena earthquake (Figure 1) and improve upon the kinematic models for that event by integrating high-precision aftershock locations, modern InSAR processing, and three-dimensional inverse modeling to define the fault geometry and slip distribution.

[3] The 13 May 1995 Kozani-Grevena earthquake struck an area of northern Greece previously considered to be of

[1]Now at Department of Earth and Environmental Sciences, Wesleyan University, Middletown, Connecticut, USA.

0148-0227/05/2004JB003263$09.00

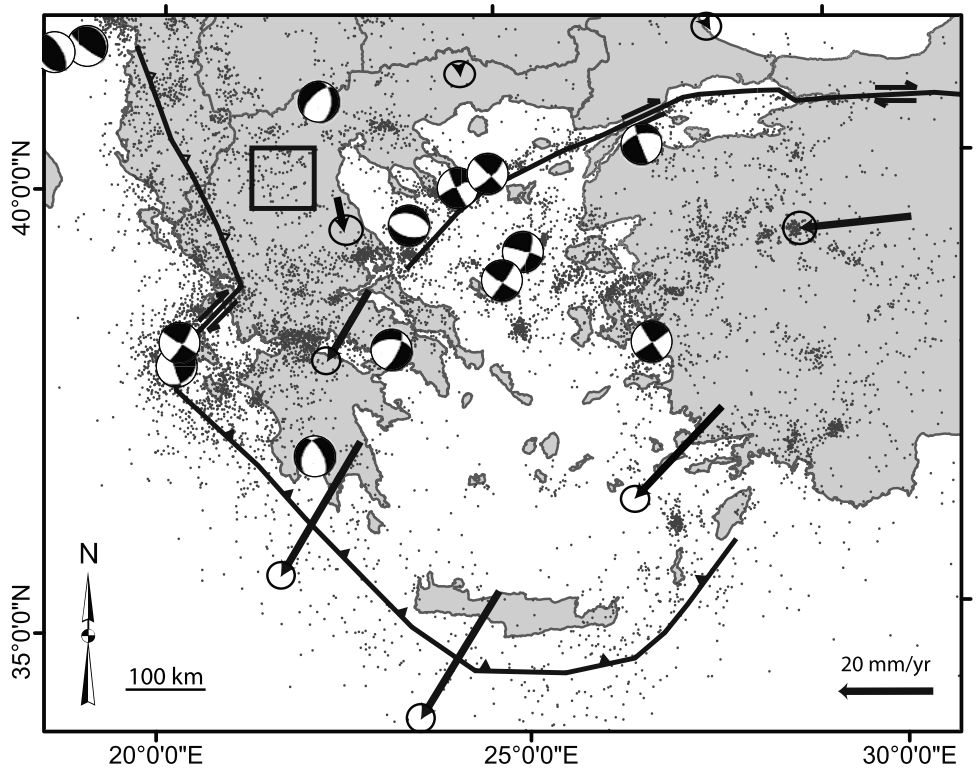

Figure 1. Seismotectonic map of the Aegean region. Major plate bounding faults are shown in bold black lines. Arrows are representative GPS velocities from *McClusky et al.* [2000]. Dots are epicenters for earthquakes M 3 or greater with source depths of less than 25 km from 1973 to 1994 (USGS NEIC catalog). Focal mechanisms are shown for events of M 6 or greater. The black box is the region illustrated in Figure 2. Projection is UTM zone 34°N.

low seismic hazard due to low historical and instrumental seismicity (Figure 1) [*Hatzfeld et al.*, 1995]. The M_w 6.5 event caused significant ground shaking and structural damage, but was associated with only minor normal sense surface rupture (Figure 2). Unambiguous tectonic fault rupture occurred along an 8-km segment of the preexisting Paleochori fault (striking 250°, dipping 70° to the northwest) to the southwest of the village of Paleochori [*Meyer et al.*, 1996] with less than 20 cm of slip down to the northwest. An alignment of possible antithetic (southeast dipping) fault-related ground disturbance was reported ~10 km north of the Paleochori fault between the villages or Rymnion and Myrsina [*Pavlides et al.*, 1995].

[4] In addition to the geological mapping of surface faulting the Kozani-Grevena earthquake was well observed geophysically. The Harvard CMT solution for the event (Table 1) had a seismic moment of 7.64×10^{18} N m, a primary nodal plane striking 243° and dipping 47° to the northwest, with a slip rake of −97° on this surface [*Dziewonski et al.*, 1996]. In addition to a relatively sparse regional seismic network, a dense local array of seismometers (Figure 2) was deployed for 7 days to record aftershocks for determining their distribution and focal mechanisms [*Hatzfeld et al.*, 1997, 1995]. Coseismic deformation of the ground surface was observed by GPS reoccupation of Hellenic Military Geographic Survey (HMGS) pillars [*Clarke et al.*, 1997] and by interferometric analysis of ERS-1 synthetic aperture radar data (InSAR) [*Meyer et al.*, 1996].

[5] Because of the relatively minor surface rupture associated with the Kozani-Grevena earthquake the subsurface fault pattern has been debated [e.g., see *Meyer et al.*, 1998] and several different subsurface fault models have been proposed. *Papazachos et al.* [1996] proposed a model for the gross geometry of the fault based on the overall distribution of aftershocks. They noted that the aftershock hypocenters formed a west-southwest striking cloud that dipped to the northwest with a length of 30 km and a width of 15 km and proposed a single fault with the same orientation and dimensions as the aftershock cloud and an average slip of 50 cm. *Hatzfeld et al.* [1997] used higher precision aftershock hypocenters recorded by a temporary local network [*Hatzfeld et al.*, 1997, 1995] to better image the subsurface fault geometry. They identified the main fault plane as a planar normal fault striking 240° west-southwest, dipping 35° to 45° to the northwest, and extending from 5 to 15 km in depth. The upper tip of this fault, as imaged by aftershocks, is located almost directly below the mapped surface rupture and the authors proposed that the ruptures may have been minor surface features associated with a largely blind coseismic rupture. *Hatzfeld et al.* [1997] also identified a second likely fault plane dipping toward the south and located to the southwest of the main fault plane. *Clarke et al.* [1997] used GPS reoccupation of Hellenic Military Geographic Survey (HMGS) pillars and nonlinear inversion methods to determine a single fault model for the Kozani-Grevena earthquake (Table 1). The planar fault model that best fit the GPS-triangulation data was a fault

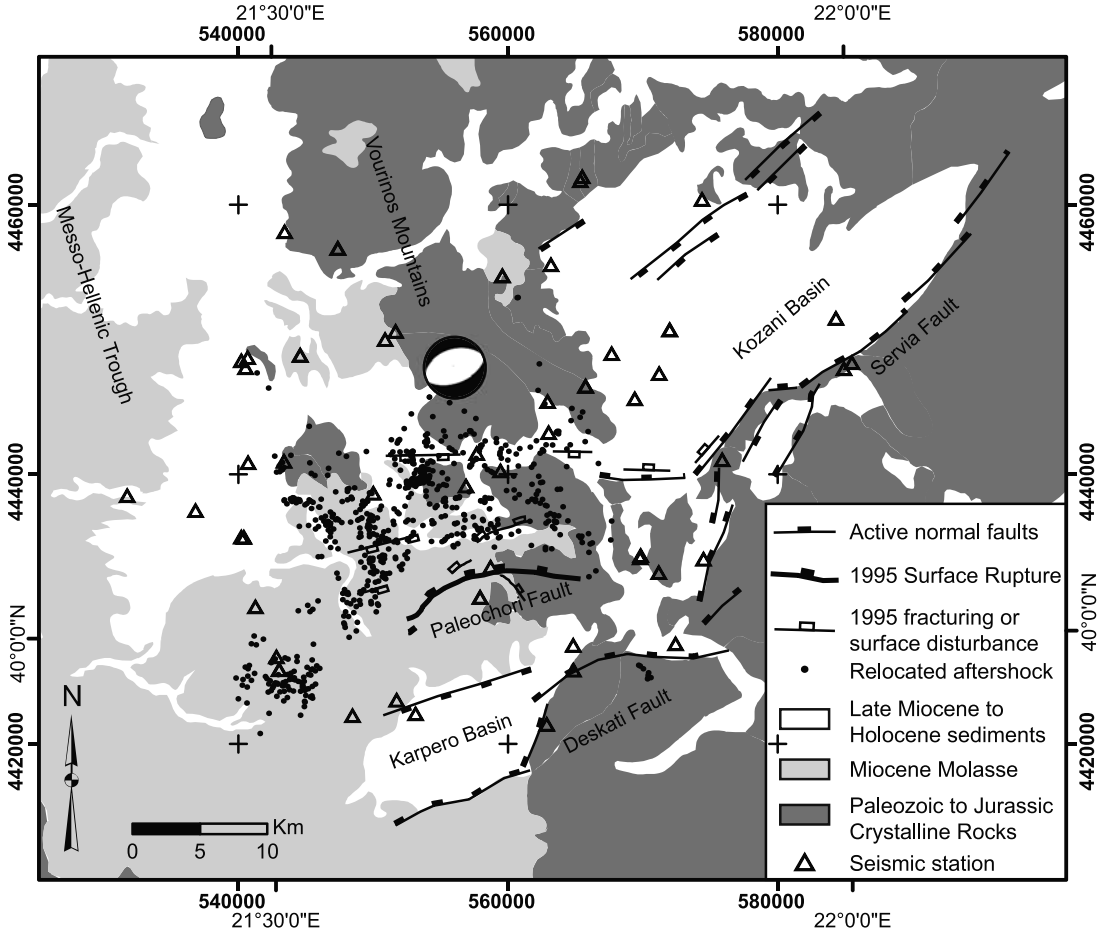

Figure 2. Structure and regional geology of the Kozani-Grevena Region. Faults are after *Doutsos and Koukouvelas* [1998] and *Meyer et al.* [1996]. Main surface rupture (modified from *Meyer et al.* [1996]) is shown in bold. Dots are relocated aftershock hypocenters. Triangles are the seismic stations of the temporary and regional networks. Geology is modified from *Mouyiaris et al.* [1989]. Projection is UTM zone 34°N.

striking 253°, dipping 43°, and extending from 2.8 to 13.5 km in depth. The modeled fault had 1.2 m of slip at a rake of −95°. *Clarke et al.* [1997] found that the GPS triangulation data alone did not require a more complicated fault model. *Meyer et al.* [1996] proposed a three-dimensional multifault model for the Kozani-Grevena earthquake based on integrated observations of surface rupture and forward modeling of a synthetic aperture radar interferogram (InSAR). *Rigo et al.* [2004] revisited the earthquake using reprocessed InSAR data, mapped surface ruptures, and the hypocenter location to constrain a three-dimensional multifault model. Their modeling strategy involved interpreting the three-dimensional fault pattern from the observed surface ruptures and the location of the hypocenter and then iteratively evaluating slip azimuth and slip distribution. Their preferred model includes a curviplanar main fault that has a smoothly decreasing dip from 65° at the surface to 22° at 14 km depth and two smaller synthetic faults near the eastern end. The maximum slip is 3 meters at the base of the western end of the fault and decreases to 4–6 cm at the surface.

[6] In this paper we integrate high-precision aftershock locations with geodetic inverse modeling to create a more

Table 1. Estimates of Kozani-Grevena Earthquake Source Parameters[a]

Method	Strike, deg	Dip, deg	Rake, deg	Moment, 10^{18} N m	Source
PDE	252	39	−86	4.7	USGS NEIC
Harvard CMT	243	47	−97	7.6	*Dziewonski et al.* [1996]
Body waveform	252	41	−87	6.2	*Hatzfeld et al.* [1997]
GPS dislocation	253	43	−95	16.3	*Clarke et al.* [1997]
InSAR iterative model	258	38	−97	6.9	*Rigo et al.* [2004]
InSAR planar	274	43	−90	13.7	this study
InSAR 3 fault	254	48	−96	14.5	this study
InSAR 5 fault	254	49	−97	14.3	this study

[a]PDE, preliminary determination of epicenters; CMT, centroid moment tensor; InSAR, interferometric synthetic aperture radar.

complete kinematic model for the Kozani-Grevena earthquake sequence. Recent advances in earthquake location methods [*Rubin et al.*, 1999; *Waldhauser and Ellsworth*, 2000] have improved relative hypocentral locations and have shown promise in imaging detailed fault structures in a variety of tectonic settings [*Chiaraluce et al.*, 2003; *Kilb and Rubin*, 2002; *Prejean et al.*, 2002; *Rubin et al.*, 1999; *Schaff et al.*, 2002; *Waldhauser and Ellsworth*, 2000]. Using slip inversion on triangular dislocation patches [*Maerten et al.*, 2005], we calculate variable slip on the imaged three-dimensional fault network that best fits the surface displacements observed by satellite interferometric synthetic aperture radar (InSAR). We compare these results to a best fitting planar fault model derived solely from the InSAR data using nonlinear inversion methods. By integrating aftershock locations, mapped surface ruptures and inverse modeling of geodetic data we mitigate problems of nonuniqueness associated with the individual data sets. High-precision aftershock locations image the three-dimensional fault structure associated with the Kozani-Grevena sequence and geodetic inversion provides a means to evaluate the contribution of the imaged faults to coseismic displacements.

2. Tectonic and Geologic Setting

[7] The Aegean region is one of the most rapidly extending continental areas today (Figure 1) [e.g., *Clarke et al.*, 1998; *McClusky et al.*, 2000; *Roberts and Jackson*, 1991]. Geodetic measurements indicate that southwestern Greece is moving toward the south-southwest at $\sim$30 mm yr^{-1} relative to Eurasia [*McClusky et al.*, 2000]. The highest rates of present-day deformation are associated with relative motions between the Anatolian, Aegean, and Eurasian plates (Figure 1) and are accommodated in the Gulf of Corinth ($\sim$12 mm yr^{-1}), across western Turkey ($\sim$10–15 mm yr^{-1}), and along the North Anatolian Fault system including the North Aegean Trough ($\sim$24 mm yr^{-1} of right-lateral motion with localized extension) [*Koukouvelas and Aydin*, 2002; *McClusky et al.*, 2000]. Localized areas of extension, however, are found throughout the Aegean from the Peloponnese in southern Greece to the Greek border with Macedonia and Albania in the northwest [*Goldsworthy et al.*, 2002]. The details of the tectonics of the region are an area of ongoing research and we refer interested readers to the many excellent studies of the topic [e.g., *Doutsos and Kokkalas*, 2001; *Jackson*, 1994; *McClusky et al.*, 2000; *McKenzie*, 1972, 1970].

[8] The 1995 Kozani-Grevena earthquake occurred along the 70-km-long Aliakmon fault zone [*Doutsos and Koukouvelas*, 1998] one of several regions of localized extension in northwestern Greece [*Goldsworthy et al.*, 2002; *Pavlides and Mountrakis*, 1987]. The region was considered to be of low seismic hazard prior to the 1995 earthquake; however, subsequent investigations have identified a number of active faults in the area based on geologic and morphologic characteristics [*Doutsos and Koukouvelas*, 1998; *Goldsworthy and Jackson*, 2000; *Meyer et al.*, 1996; *Mountrakis et al.*, 1998]. The Aliakamon fault system (Figure 2) strikes northeast-southwest and is composed of a series of echelon segments ranging from approximately 5 to 20 km in strike length [*Doutsos and Koukouvelas*, 1998; *Goldsworthy and Jackson*, 2000]. The major faults principally dip to the northwest from 60° to 80°; however, southward dipping (antithetic) faults are found in the hanging wall of the major faults in a number of locations, particularly in the Kozani and Karpero basins [*Doutsos and Koukouvelas*, 1998]. In the western half of the fault system, where the Kozani-Grevena earthquake occurred, the fault system is composed of at least two major strands, the Paleochori fault that continues roughly along strike of the eastern (Servia) faults and the Deskati Fault which branches off into the footwall of the Servia fault. The overall strike of the fault system changes from $\sim$230° for the eastern segments, to $\sim$260° for these western segments. *Doutsos and Koukouvelas* [1998] estimated the total displacement across the various segments of the fault system using scaling and flexural arguments. These authors estimated a maximum slip of $\sim$2000 m for the Servia fault system adjacent to the Kozani basin with lesser slip in the overlap zone with the Deskati fault including the Paleochori segment. *Goldsworthy and Jackson* [2001] estimated 120 m of throw for the Paleochori fault based on extrapolation of a surface slope in Neogene sediments. The segments of the Aliakmon fault system with the largest throw have localized small basins in their hanging walls. These basins are Pliocene and younger and are filled with fluvial and lacustrine sediments [*Doutsos and Koukouvelas*, 1998]. In the Kozani basin these sediments exceed 600 m in thickness.

[9] The Aliakmon fault system cuts across the preexisting tectonic grain associated with the Eocene to Miocene collision of the Apulian platform and Pelagonian microcontinent, part of the broader alpine collision [*Doutsos et al.*, 1994; *Mountrakis et al.*, 1998]. The fault system is thus developed in a variety of rock types (Figure 2) and has variable surface expression along strike [*Goldsworthy and Jackson*, 2001]. In the eastern to central portions of the fault system the Vourinos massif exposes Paleozoic-Triassic metamorphic rocks and Jurassic ophiolites that were thrust onto the Apulian platform. These basement rocks are overlain unconformably by Jurassic carbonates. Normal fault segments in this portion of the fault system, such as the Servia and Deskati faults, have prominent scarps and footwall uplifts typical of active faults throughout Greece [e.g., *Armijo et al.*, 1996]. The western portion of the fault system cuts the Messo-Hellenic Trough, a 130-km-long, 30-km-wide basin filled with up to 3500 m of molassic sediments that is interpreted to have formed as a piggyback basin during alpine collision and postorogenic collapse from the Oligocene to Miocene [*Doutsos et al.*, 1994]. Scarps associated with active normal faults that cut the Messo-Hellenic trough are much more subdued [*Goldsworthy and Jackson*, 2001].

3. Aftershock Relocations

[10] The double-difference algorithm [*Waldhauser and Ellsworth*, 2000] allows for calculation of high-precision hypocentral locations for events whose separation is small compared to the distance between the events and the seismic stations. The method assumes that the ray paths between adjacent events and distant receivers is essentially the same and therefore attributes differences in arrival times solely to

Table 2. One-Dimensional Velocity Model[a]

Depth, km	V_P Velocity, km s^{-1}	V_s Velocity, km s^{-1}
0.0	4.200	2.4277
2.0	5.000	2.8902
5.0	5.300	3.0636
11.0	5.800	3.3526
15.0	6.200	3.5838
23.0	6.500	3.7572
30.0	7.350	4.2486

[a] V_p/V_s is set to a constant ratio of 1.73.

the spatial separation between events. Hypocentral locations are adjusted iteratively to minimize the residual between predicted and observed travel time differences for pairs of earthquakes observed at common stations. By simultaneously adjusting all pairs of adjacent (linked) events the method improves relative locations for all linked events. The centroid of the relocated aftershocks is constrained to remain at the centroid of the original locations; however, this constraint is applied loosely so that there is some sensitivity to absolute location of the aftershock cluster [*Waldhauser and Ellsworth*, 2000].

[11] We have applied the double-difference algorithm to relocate aftershocks recorded by a temporary local seismic network of 40 instruments that was set up after the Kozani-Grevena earthquake (Figure 2) and recorded >600 aftershocks between 19 May 1995 and 25 May 1995 [*Hatzfeld et al.*, 1997, 1995]. Because of the favorable network geometry, including both near-source receivers and good azimuthal distribution, these data offer the best possibility for imaging the fault system associated with the Kozani-Grevena earthquake. 668 of these events were located by *Hatzfeld et al.* [1997] using standard location techniques with station corrections and 662 have hypocentral errors of <1 km. Although the permanent regional networks (Thessaloniki and National Observatory of Athens) also recorded many of the same events, as well as the rest of the seismic sequence including the foreshock, main shock, and largest aftershocks, the geometry of these networks is not adequate for determining high-precision locations. A comparison between events recorded by the regional network prior to the deployment of the local network (13–18 May 1995) and those recorded during deployment of the local network (19–25 May 1995) showed no significant differences between the distribution of events immediately after the main shock and those that occurred during the time period that the local network was deployed. The local network data thus appear to be representative of the structures active during the first weeks of the Kozani-Grevena seismic sequence.

[12] We used over 16,000 P and S wave phase picks of *Hatzfeld et al.* [1997] for 668 events recorded by the local network to calculate difference times for 136,209 P wave pairs and 7176 S wave pairs. Initial difference times were calculated for events closer than 10 km including up to 50 of each event's nearest neighbors. We used the existing locations [*Hatzfeld et al.*, 1997] for pairing earthquakes when calculating difference times and as initial locations for the double-difference algorithm. Individual arrival picks were weighted relative to predetermined pick quality (0–4), and S arrivals were weighted half of P arrivals due to the difficulty of picking S wave arrivals within the coda. Travel time derivatives were calculated using a one-dimensional velocity model derived from the same set of events by *Draktos et al.* [1998] and a V_p/V_s ratio of 1.73 (Table 2). After five iterations events with more than 6-ms residuals and event pairs with more than 4-km separations were dropped for calculating the final locations.

3.1. Relocation Results

[13] Using the double difference algorithm, we relocated 650 of the initial 668 events. To estimate hypocentral location errors, we relocated a subset of the data using a singular value decomposition (SVD) [*Chiaraluce et al.*, 2003; *Waldhauser and Ellsworth*, 2000]. Hypocentral errors for this subset of 171 events were improved by a factor of ~7. The initial aftershock locations determined using traditional methods had horizontal and vertical errors of less than 1000 m [*Hatzfeld et al.*, 1997] while double difference locations have errors of less than 150 m.

[14] In Figure 3a we present the map view of the local seismic network and relocated aftershocks with vectors indicating the change of hypocentral location in relation to previously determined positions. The largest changes in location are generally found for events near the periphery of the network while events in the center of the cluster are moved less. A similar result was reported by [*Chiaraluce et al.*, 2003] for the Colfiorito earthquake sequence, Italy. In Figure 3b the relocation results are visualized in two cross sections through the main and southwest clusters with both preexisting and relocated aftershocks. These cross sections project data from a 4-km-wide swath parallel to the section line. In both cross sections the gross structure could be inferred from the existing locations; however, the new locations provide a better image of the fault structure and admit a more precise interpretation of the fault surfaces. In section A-A′ the relocated aftershocks define a northward dipping surface with two southward dipping (antithetic) surfaces that intersect near the midpoint and the upper tip of the northward dipping surface. In section B-B′ the southwest cluster that *Hatzfeld et al.* [1997] inferred to be an antithetic fault now more clearly defines a surface dipping steeply to the southwest. The 55° dip of this surface is consistent with the average focal mechanism for these events calculated by *Hatzfeld et al.* [1997].

[15] Figures 4 and 5 present insightful views of the entire set of relocated aftershocks. In map view (Figure 4a) the majority of aftershocks are distributed in an arcuate pattern that spans ~25 km east-west by ~25 km north-south. The southern edge of this arcuate distribution parallels the mapped surface ruptures with ~3 km horizontal separation between the cutoff in seismicity and the surface faulting. The red-yellow-green banding, seen most clearly near the eastern margin of the seismicity, shows that the aftershocks describe a northward dipping surface. This surface can be seen more clearly by viewing the aftershock cluster from an oblique aerial view looking northward and down from an angle of 40° (Figure 4b). Two distinctly separate clusters are located to the southeast and southwest of the main group. The southeast cluster is composed of eight tightly clustered events. The southwest cluster is made up of ~90 events that increase in depth to the south.

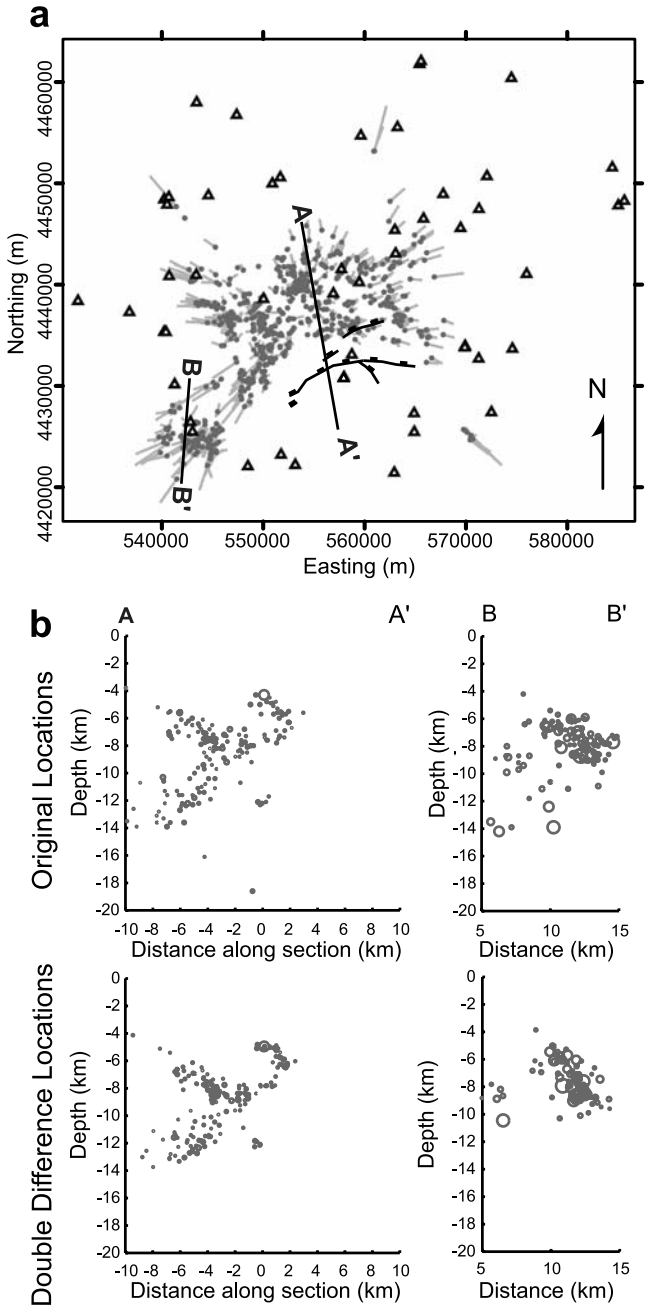

Figure 3. (a) Map showing vectors between original aftershock locations [*Hatzfeld et al.*, 1997] and new locations, marked by dots. Triangles are seismic stations used for aftershock location. Coseismic surface ruptures (solid lines) are modified from *Meyer et al.* [1996]. Lines A-A′ and B-B′ are location lines for cross sections illustrated in Figure 3b. (b) Cross sections comparing (top) previous locations and (bottom) new locations.

[16] The detailed structure of the seismicity is best illustrated in a series of cross sections (Figure 5) constructed by projecting hypocenters from 4-km swaths onto section lines shown in Figure 4. Sections 1–8 are oriented north-south while sections 3b–5b are oriented 40° NW. All sections are presented at equal vertical and horizontal scales and are viewed from the west or southwest. Sections 1 and 2 show a clear alignment of aftershock hypocenters in the southwestern cluster (located at the southern end of the cross sections) that dips ~55° to the south. In addition, a vertical alignment of hypocenters can be seen near the northern end of section 2. Sections 3 and 3b do not show a clear alignment of hypocenters; however, there is a poorly aligned near-vertical cluster of aftershocks at the southeast end of section 3b. In sections 4–7, aftershock hypocenters increase with depth northward, forming an alignment that dips ~40°. This trend is best defined at the base of the seismicity with more diffuse seismicity above this line. The seismicity is more diffuse in section 7 at the eastern end of the main aftershock cluster. In section 4, near the bend in both the surface ruptures and the main aftershock cluster, the seismicity is more diffuse and the apparent dip of the aligned hypocenters is lower than in sections 5 and 6.

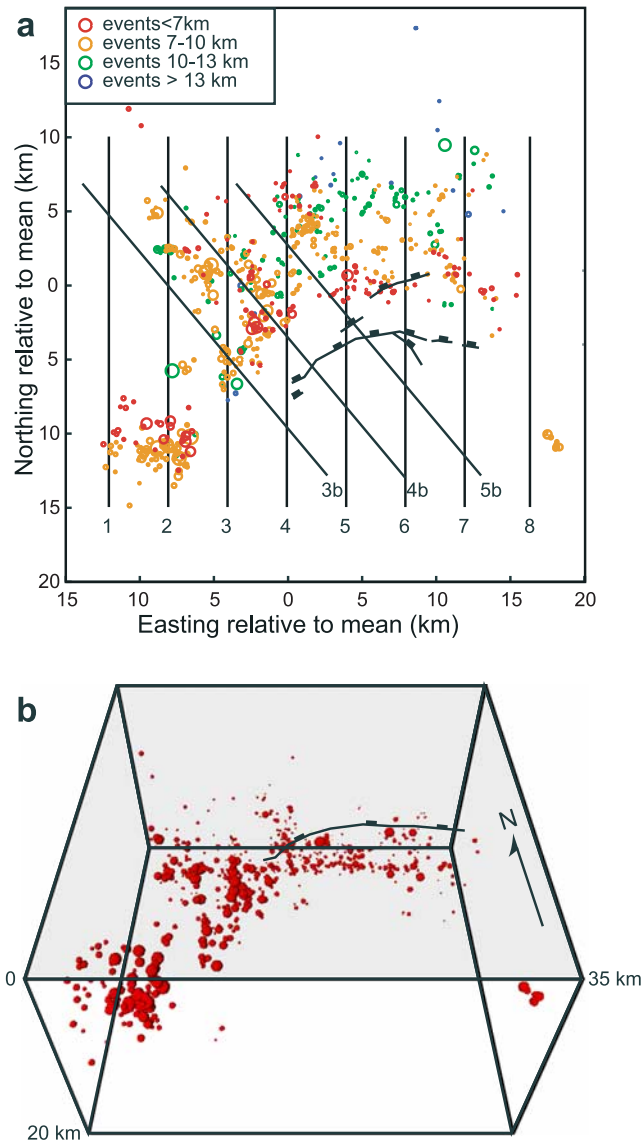

Figure 4. (a) Map of relocated aftershock hypocenters with cross section lines. Circle diameter represents relative event magnitude (1–3.9). Events in map view are color coded by depth. (b) View to the north at an angle of 40° from horizontal.

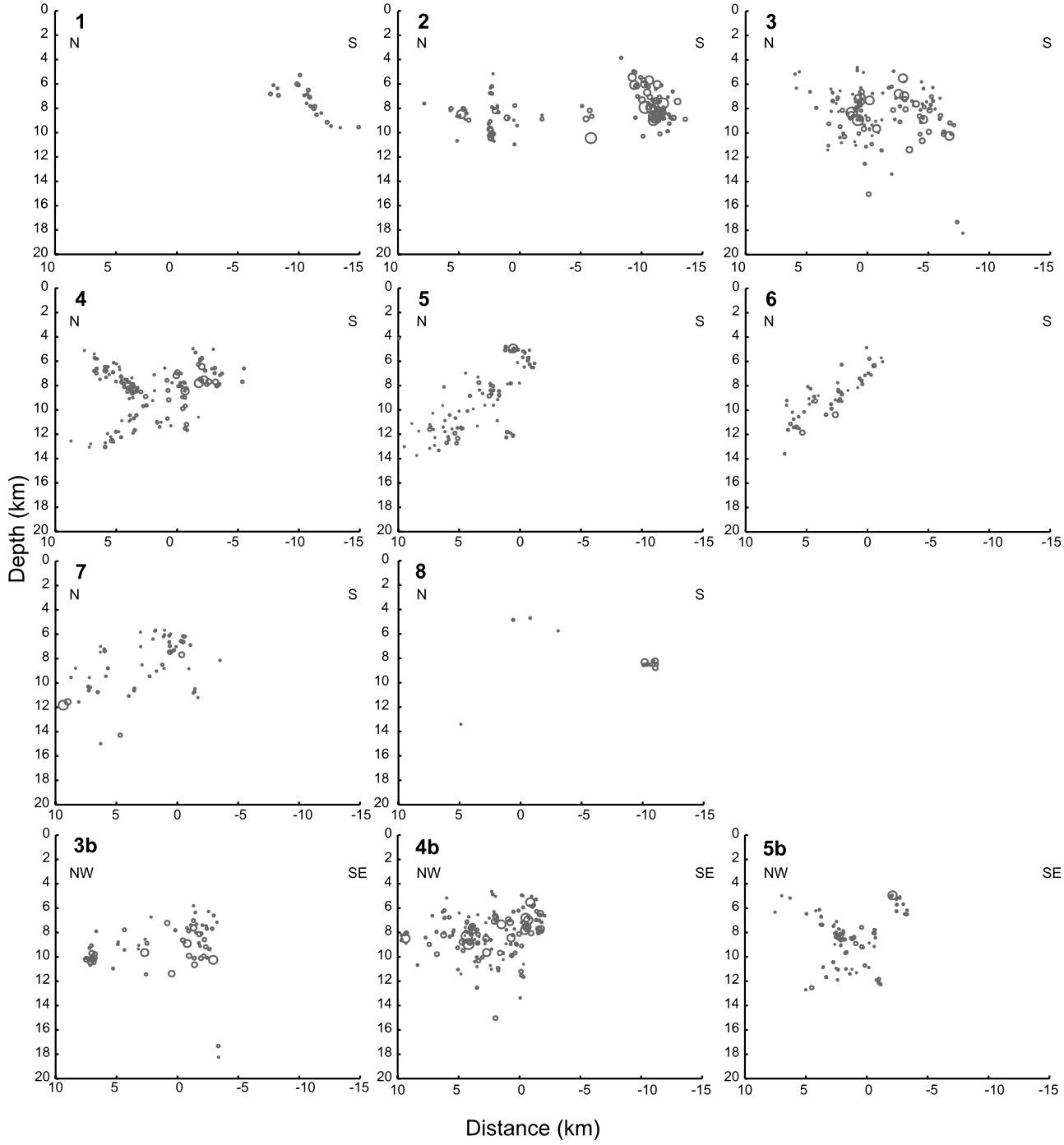

Figure 5. Serial cross sections through relocated aftershocks (see Figure 4 for locations). Circle diameter represents relative event magnitude (1–3.9). Sections 1–8 are oriented north-south. Sections 3b–5b are oriented N40°W. All sections are 1:1, units are km, and sections project 4-km swath of data parallel to the section line.

Sections 4b and 5b, oriented at 40°NW, image a more steeply dipping surface, consistent with sections 5–7.

3.2. Fault Interpretation

[17] We interpret the alignments of aftershocks described above as fault surfaces active during the Kozani-Grevena earthquake sequence. The major interpreted fault surfaces are presented in a three dimensional model, two views of which are presented in Figure 6. The aftershock patterns image a nearly west striking master normal fault that dips ~43° from ~6 km to ~15 km depth. The main fault extends ~20 km along strike and is slightly convex to the north along strike. At approximately the location of section 4 there is either a kink or intersecting fault. We favor the intersecting fault geometry as the east-west trend of aftershocks appears to continue beyond this point to the west (best seen in Figure 4b). The southwest striking segment is poorly imaged in sections 3b and 4b but appears to dip more steeply toward

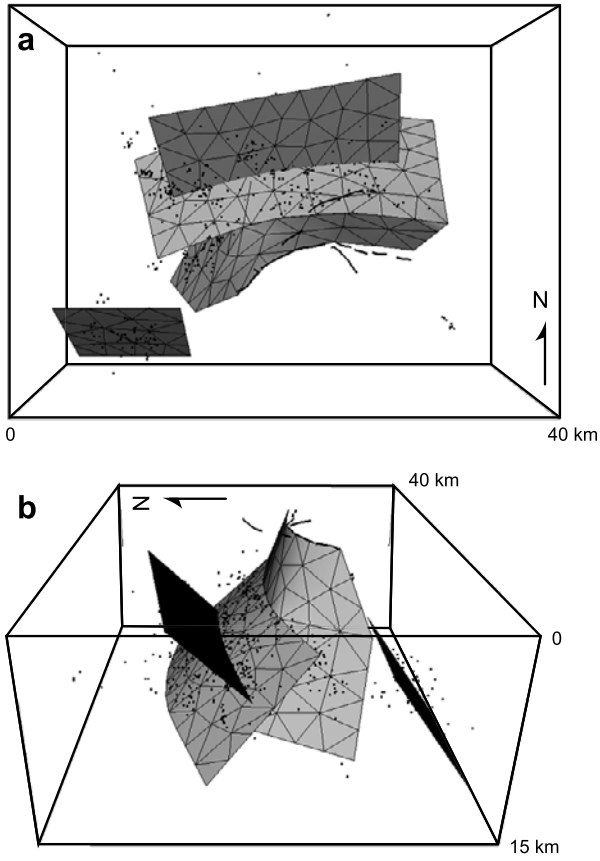

Figure 6. Three-dimensional fault model interpreted from aftershock locations. (a) Top view. (b) Oblique view from above west. Dots are aftershock hypocenters. Black lines on upper surface are observed ruptures [*Meyer et al.*, 1996].

the northwest. We interpret this fault to strike ~210° and dip ~65° to the northwest. The updip tip of these two fault segments, as imaged by aftershocks, could connect to the surface ruptures by a fault dipping 70°. This upper fault segment is not imaged, but is inferred based on the observed surface faulting. To the southwest of the main aftershock cluster is a clearly imaged east striking fault that dips ~55° to the south. The extent of this fault, as imaged by aftershocks, is from ~4 km to ~10 km in depth with a strike length of ~6 km. An antithetic fault is clearly imaged in section 4 dipping ~40° to the south and is also poorly imaged on the northern end of section 3 (it is also seen in the overlapping section 5b). This fault extends from ~5 to ~9 km depth and strikes to the east over ~5 km. A second smaller antithetic fault is well imaged at the updip tip of the master fault in section 5 and appears to be poorly imaged in section 4. This fault also dips ~40° and extends from ~4 to ~6 km depth. Apparent vertical faults are imaged near the northern ends of sections 2 and 3, but do not extend onto other cross sections. These faults extend from 5 to 11 km depth.

4. Comparison to Observed Coseismic Deformation

[18] In order to evaluate proposed fault models for the Kozani-Grevena earthquake, and to construct a more complete kinematic model for the event we have performed inversions for fault geometry and slip using interferometric synthetic aperture radar (InSAR) data that span the event. Coseismic deformation was observed both by radar interferometry [*Meyer et al.*, 1996] and GPS reoccupation of a regional triangulation network [*Clarke et al.*, 1997] We have chosen to focus here on the InSAR data due to uncertainties associated with the preexisting triangulation survey (P. Clarke, personal communication, 2004). We use different SAR data and processing methods to those of *Meyer et al.* [1996] and the resulting interferogram more clearly images the coseismic deformation than the previously published images.

4.1. Coseismic Interferogram

[19] The coseismic deformation of the 1995 Kozani-Grevena earthquake has been mapped using an interferogram that spans the event, formed from ERS-1 images acquired on 16 November 1993 and 9 November 1995. The images were acquired on a descending satellite pass, and have an average perpendicular baseline of just 3 m, smaller than the 70 m baseline of the pair used by *Meyer et al.* [1996], with which we have one scene in common (16 November 1993 to 5 October 1995). Despite the longer time span of our preferred interferogram, the shorter baseline results in a significant improvement on interferometric coherence. Where the two interferograms are both coherent, the difference between the interferograms is small (RMS difference of 11 mm) and largely correlated with surface topography, suggesting that it is atmospheric in origin rather than being the result of postseismic deformation.

[20] The InSAR data is irregularly distributed due to decorrelation, principally in the lowland areas (Figure 7a). The coseismic deformation is thus imaged discontinuously with the eastern end of the affected area well imaged and the western end more poorly imaged. The phase data have been filtered [*Goldstein and Werner*, 1998] and unwrapped to derive the displacement field in the satellite's line of sight (Figure 7b), which has an average unit look vector of (−0.385, 0.079, 0.919). The interferogram describes a broad area of increased range (primarily subsidence) approximately 30 km by 20 km with the long axis oriented east-west and a maximum range increase of ~70 cm. The area of subsidence is roughly centered on the mapped surface ruptures in an east-west sense but begins approximately 1–2 km south of the mapped surface ruptures and extends to the north. An area of range decrease (primarily uplift) of ~10 cm is located south of the mapped surface ruptures but is not as well imaged by the InSAR data. Two displacement discontinuities are imaged, one along the eastern trace of the Paleochori fault (UTM zone 34 coordinates in meters: 5.62×10^5 east, 4.430×10^6 north) and another within the Vourinos Mountains near the northern edge of the area of range increase (UTM zone 34 coordinates in meters: 5.60×10^5 east, 4.445×10^6 north). The first discontinuity is located ~0.5 km north of the mapped coseismic surface rupture along the Paleochori fault [*Meyer et al.*, 1996]. This part of the rupture was mapped as an approximate location (dashed), and we have adjusted the location in our figures and models to reflect the location imaged by the InSAR data. We interpret the second discontinuity as a southwestward dipping normal fault on which there was shallow

triggered slip during the Kozani earthquake leading to a narrow zone of subsidence to the southwest of the discontinuity (fault). The discontinuity is ~10 km in length, strikes to the southeast and is associated with an area of localized range increase ~2 km wide. This feature is found on all published interferograms for the Kozani earthquake [*Meyer et al.*, 1996; *Rigo et al.*, 2004].

[21] The unwrapped, cropped interferogram (Figure 7b) has almost 3 million data points. In order to expedite inversions using the InSAR data we have decimated the data using a quadtree approach [e.g., *Welstead*, 1999]. The quadtree algorithm divides the data into quadrants and continues to subdivide each quadrant until a defined criterion or minimum size is reached. We have followed the approach of *Jónsson et al.* [2002] using the scatter about the mean as our division criterion. If the scatter about the mean of a data quadrant exceeds the half wavelength of the radar (2.83 cm) the quadrant is subdivided further. This approach reduces the overall number of data without significantly reducing the statistical significance of the radar interferogram signal [*Jónsson et al.*, 2002]. The resulting decimated grid (Figure 7c) has 389 data points that represent the mean for blocks varying in size from 512 × 512 pixels (20.48 km × 20.48 km) to 8 × 8 pixels (0.32 km × 0.32 km). Blocks that contained less than 50% data values were assigned a no data value.

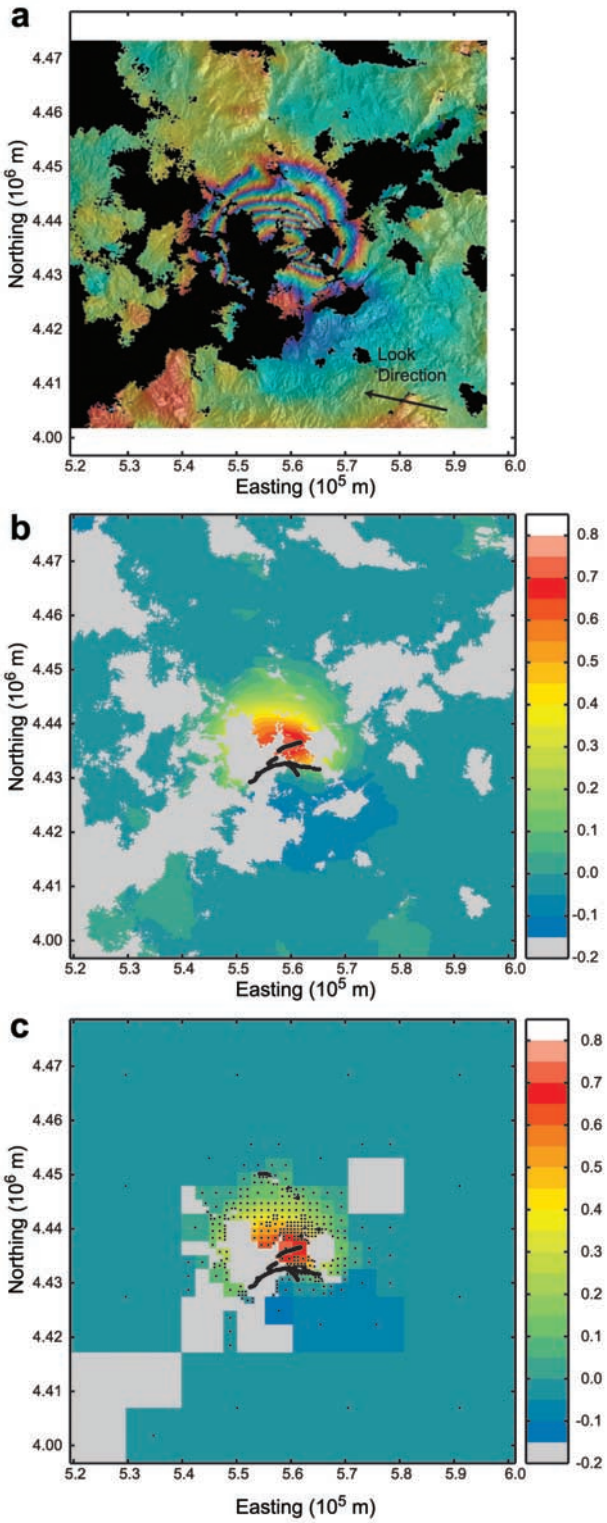

Figure 7. InSAR data. (a) Interferogram rewrapped so that each fringe is equivalent to 10 cm of deformation in the satellite's line of sight. (b) Unwrapped displacement data with a uniform 16-cm shift associated with processing errors removed. (c) Quadtree gridded data used for inversions. The colored boxes illustrate the bins used to calculate the decimated data set, while the black points show the actual positions of the final data points used for the inversions.

4.2. Modeling Coseismic Deformation

[22] Deformation at the earth's surface can be related to fault slip at depth through a system of equations of the form

$$\mathbf{d} = \mathbf{G}(\mathbf{m}) + e, \tag{1}$$

where **d** is the vector of observed displacements, **m** is the fault model and includes both geometric parameters (fault dimensions, position, and orientation) and fault slip parameters (strike slip, dip slip, and opening), **G** is the function that describes the relationship between the model and observations, and e is the measurement error. This set of equations is linear in slip, but nonlinear for fault geometric parameters.

[23] Taking equation (1) as an inverse problem, fault parameters (**m**) can be estimated using surface deformation observed by InSAR (**d**). We seek the best fitting model, i.e., the model that minimizes the L2 norm of the data residual,

$$\min\|\mathbf{G}(\mathbf{m}) - \mathbf{d}\|_2. \tag{2}$$

In this paper we take a stepwise approach, first solving the general nonlinear problem for the simplified geometry of a rectangular dislocation in an elastic half-space [*Okada*, 1985] and then performing linear inversions for heterogeneous slip on both the best fitting planar fault and on the three-dimensional fault geometry interpreted from the aftershock patterns and surface ruptures. This approach allows for statistical comparison between models based purely on the InSAR data and geometric models based on multiple independent data sets.

[24] To solve the nonlinear inverse problem, we use a simulated annealing approach described and coded by *Cervelli et al.* [2001]. This approach seeks the global minimum within a complex misfit space by running a series of iterations at various "temperatures" where the temperature determines the degree of randomness in the search. At high temperatures the search is essentially random, while at low temperatures the search is highly directed, based on the local probability distribution. A cooling schedule is applied to progress from a nearly random search, where a wide variety of models are tested, to a more directed search where the best fit is found within the vicinity of the global minimum. Most of the search time is spent near a critical temperature where the global minimum is defined. Final models are refined using a derivative-based method to find the absolute minimum in the vicinity of the global minimum defined by the annealing method.

[25] The model we use is a single rectangular elastic dislocation in an elastic half-space (disloc, a C-language code written by P. Cervelli and based on work by *Okada* [1985]). We solve for 12 parameters: fault location (x and y), width, height, depth, strike, dip, strike-slip magnitude, and dip-slip magnitude, plus three tilting parameters to account for unmodeled errors in the orbital parameters associated with the InSAR processing.

[26] Although the highly simplified geometry described above is needed for computational efficiency in the case of nonlinear inversion, it is unlikely to represent the true complexity of the fault system associated with the Kozani-Grevena earthquake. The distribution of aftershocks and mapped surface rupture pattern suggest a three-dimensional fault pattern including multiple segments with varying strikes and dips. By postulating a fault geometry a priori from nonlinear inversion, aftershock distributions, surface breaks, or some combination of these approaches, and inverting for slip on the given fault surfaces, equation (1) can be reduced to a system of linear equations. Solving the linear problem is more efficient computationally and thus allows for discretization of faults into smaller triangular elements to calculate variable slip and to honor the three-dimensional geometry.

[27] Many previous studies [e.g., *Harris and Segall*, 1987; *Johnson et al.*, 2001; *Jónsson et al.*, 2002] have discretized fault surfaces into multiple rectangular slip patches. We have chosen to use triangular elements because of their ability to more accurately model three-dimensional geometry without introducing overlaps or gaps [*Maerten et al.*, 2005]. The approach uses the analytical solution for an angular dislocation in an elastic half-space [*Comninou and Dunders*, 1975] to construct triangular dislocation patches. When inverting for slip on multiple dislocation patches a second term is included in the minimization to simultaneously reduce the roughness in the model, in addition to the data residual. Roughness is defined as the change in fault slip per fault area and is typically reported in units of cm km^{-2} [*Harris and Segall*, 1987]. The minimization problem thus becomes

$$\min\left[\|\mathbf{Gm}-\mathbf{d}\|_2+\varepsilon^{-2}\|\mathbf{Dm}\|_2\right], \tag{3}$$

where the model roughness term, $\varepsilon^{-2}\|\mathbf{Dm}\|_2$, is composed of a scalar smoothing parameter ε multiplied by the L2 norm of a discrete second-order difference operator **D**. The value of ε controls the amount of smoothing and may be determined either from a trade-off curve, seeking to balance smoothing with data fitting, or by cross validation [*Du et al.*, 1992; *Harris and Segall*, 1987]. Equation (3) is solved using a constrained least squares approach [*Lawson and Hanson*, 1974].

4.3. Inversion Results

[28] The best fitting rectangular dislocation source for the decimated InSAR data set is a surface striking 274°, dipping 43° north, with a constant slip of 1.8 m over an area extending 16.7 km along strike and 14.9 km downdip. The top of the dislocation is located at 2.5 km depth below the half-space surface. Inversions including strike-slip result in only small strike-slip components and do not significantly improve the fit to the data; therefore the final model is constrained to be pure dip slip. These results are consistent with seismically determined focal mechanisms that calculate an inconsistent and small component of oblique slip (Table 1).

[29] The best fitting single dislocation is located to the north of, and above, the fault surface imaged by the relocated aftershocks. It roughly parallels the surface defined by the eastern half of the aftershocks. The resulting single dislocation source is also inconsistent with teleseismic focal mechanisms that determine a more southwesterly striking fault plane solution (Table 1). This discrepancy is due to the fact that the solution is strongly controlled by the data at the eastern end of the rupture where the aftershocks image a nearly east-west plane. The poor data coverage at the western end of the rupture does not place a strong constraint on the final solution. These results illustrate the need for a nonplanar model to explain all of the available data.

[30] The results of linear slip inversions allow for evaluation of the fault model interpreted from the aftershock distribution and the best fitting planar model derived solely from the InSAR data. Figure 8 presents slip inversion results, forward modeled (predicted) range change and data residuals for three models: the best fitting planar fault model (Figure 8a); a three-segment model that incorporates the primary structures interpreted from the aftershock relocations (Figure 8b); and a five-fault model that incorporates all of the significant structures interpreted from the aftershocks (Figure 8c). The results of each of these models are discussed in more detail below. These models were constructed with nearly equal numbers of elements, and thus approximately equal numbers of free model parameters, to facilitate statistical comparison. The incorporation of the three-dimensional fault model based on aftershock interpretations (Figure 8b) leads to a 50% reduction in the residual sum of the squares when compared to the planar fault model (Figure 8a).

[31] The planar fault model (Figure 8a) was constructed by creating a fault that was coincident with the best fitting single dislocation model, but was expanded to allow for a broader area of lower slip permitted by the variable slip model. The planar fault extends from 0.5 km to 14.7 km in depth and has a width of ~25 km. The model is discretized into 143 elements that average 3.7 km^2 in area.

[32] Slip inversion results show broadly distributed slip with a maximum of 2.6 m near the upper eastern corner of

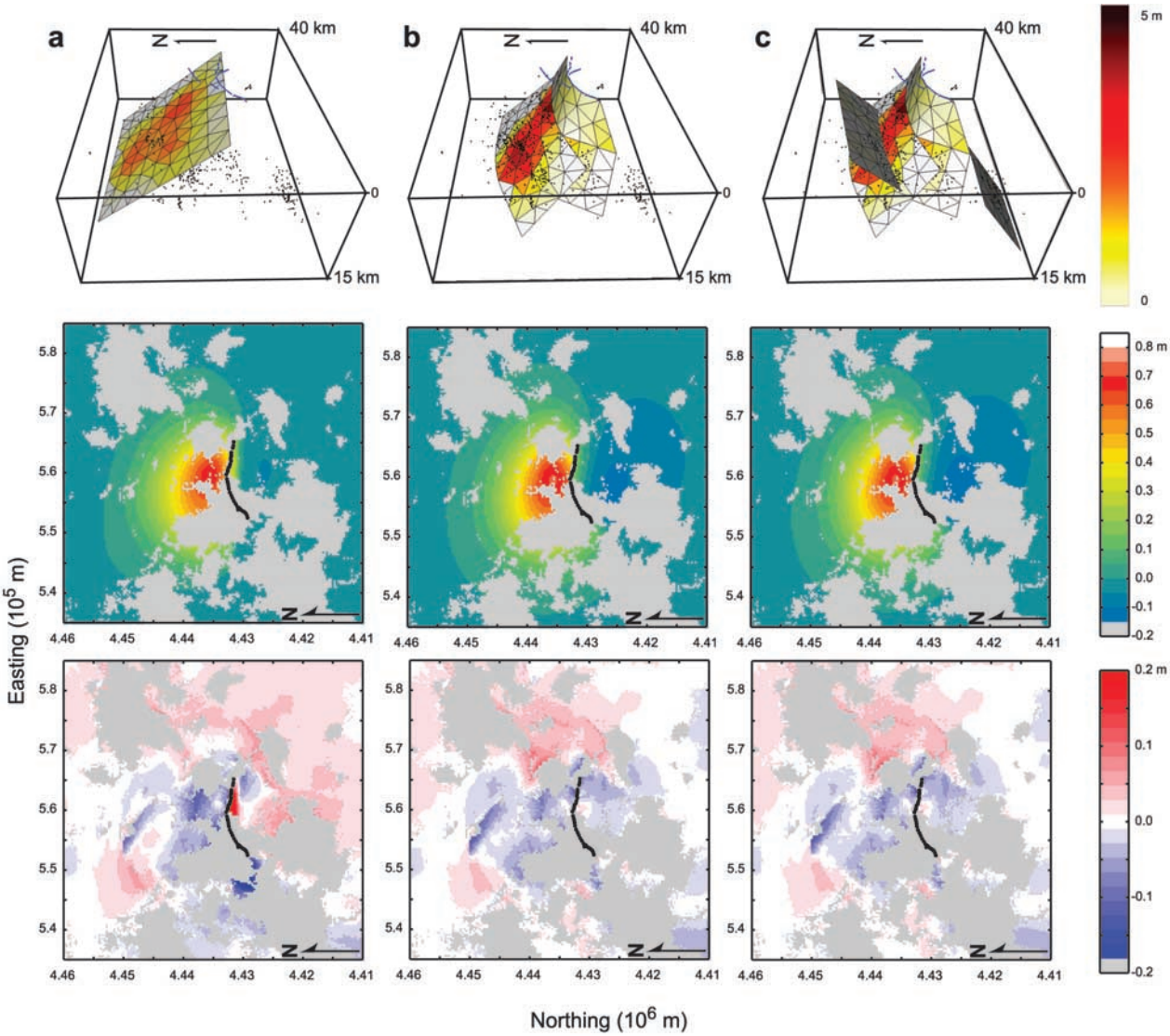

Figure 8. Inversion results for three models (left to right): (a) the best fit planar model from nonlinear inversion, (b) a three-fault model including major fault segments interpreted from aftershock hypocenters and surface ruptures, and (c) a five-fault model including two antithetic faults also interpreted from aftershock distributions. For each model, three images are presented: (top) an oblique view of the model looking toward the east from an angle of 45° with the slip distribution calculated from linear inversion of InSAR data, aftershock hypocenters, and surface rupture traces; (middle) the results of the forward model illustrating predicted surface deformation (range change) with areas of no InSAR data in gray; and (bottom) the calculated residuals for each model. Note that north is toward the left in all images.

the fault. The predicted range change for the planar fault shows a subsidence pattern that is grossly similar to the observed deformation. The RMS error for this model is 4.53 cm. In general the model underpredicts the hanging wall subsidence and footwall uplift. The largest misfits (up to 22.4 cm) can be seen in the residual along the eastern portion of the surface rupture and in the hanging wall near the western end of the rupture. The misfit in the east is likely due to the lack of inclusion of the surface rupture in the model. The misfit in the west, however, is due to the inability of a planar model to fit both the eastern and western ends of the area of subsidence. At the western end of the imaged deformation, the area of subsidence clearly wraps around to the southwest.

[33] The three-fault model (Figure 8b) incorporates the major fault segments interpreted from the aftershock data and the surface ruptures. The model includes the large curviplanar westerly striking segment, the more steeply dipping southwest striking segment, and the upper fault segment described previously. These fault segments are discretized into 154 elements with an average size of 3.8 km^2.

[34] Slip inversion results model the highest slip values on the deep westerly striking segment. The area of high slip is distributed from the upper tip at the eastern end to the middle of the lower tip with a maximum slip of 4.7 m near the upper tip. The southwest striking segment has a maximum slip of 2.2 m at its intersection with the westerly

striking fault with decreasing slip to the southwest. The upper segment has a maximum slip of 0.8 m located in the bend region near the surface. These values are not constrained by near-field data and exceed the observed surface slip. Because the elements use averaged values of slip over fairly large areas we have not chosen to impose surface slip values. The highest slip values are generally located near the fault bend with a secondary maximum at the lower southwest tip.

[35] Predicted range change for the three-fault case (Figure 8b) shows an area of subsidence that wraps around to the southwest, more closely matching the broad pattern of observed deformation than the planar fault model. The RMS residual for the model is 3.06 cm. The largest residuals (15.0 cm) are on the northern and eastern margins of the area of subsidence, and appear to be associated with local high-frequency features, possibly small-scale faults, landslides, or topographic effects. The footwall subsidence is slightly underpredicted and hanging wall uplift is slightly overpredicted.

[36] The five-fault model (Figure 8c) includes the faults from the three fault model as well as the antithetic faults in the hanging wall of the westerly fault and the fault to the southwest of the main fault system. This model was constructed to evaluate the possible contribution of these faults to the overall deformation. The slip pattern on the three faults is similar to that in the three fault model with a maximum of 4.8 m of slip on the west striking fault, 2.5 m of slip on the southwest striking segment and 0.8 m of slip on the upper segment. The hanging wall antithetic fault has greatest slip on the western and eastern ends with a maximum of 0.3 m near the eastern up dip corner of the fault. The southwestern fault has only 0.2 m of slip on its eastern edge. Although there is poor data coverage near this fault, there is no clear evidence of significant deformation in the area. The overall predicted range change pattern and residuals for the five-fault model are similar to the three fault model. The RMS error for the model is 3.04 cm with a maximum residual of 14.9 cm. The main difference is just north of the subsidence maximum where the contours of subsidence have a straighter east west trend rather than a strongly curved shape. This effect can also be seen in the InSAR data and the inclusion of the hanging wall antithetic fault leads to a slightly reduced residual in this portion of the interferogram.

5. Discussion

[37] In this study we have taken a different approach to previous investigations of the Kozani-Grevena earthquake in our method for interpreting the subsurface fault pattern, our InSAR data processing, and modeling of the deformation. Using high-precision aftershock locations, we have reduced hypocentral location errors by a factor of ~7 and thus imaged the details of the fault structure associated with the Kozani-Grevena earthquake sequence. Previous models were based on the broad distribution of aftershocks [*Hatzfeld et al.*, 1997; *Papazachos et al.*, 1998] or the projection of surface rupture patterns to depth [*Meyer et al.*, 1996; *Rigo et al.*, 2004].

[38] We have constructed a multisegment fault model based on our interpretation of the fault pattern. This model includes a master normal fault that strikes nearly due west and dips toward the north at 43°, extending from 6 to 15 km depth. This segment is connected to the surface ruptures by an inferred 70° dipping upper segment that is aseismic during the period of time that the local seismic network was in place. Additional fault segments include hanging wall antithetic faults, a more steeply dipping southwest striking linking structure at the southwest end of the rupture, and a separate south dipping segment at the southwestern end of the aftershock cluster. For the master fault we prefer a kinked geometry between two relatively planar segments in cross section rather than a smoothly curving (listric) single fault surface [*Rigo et al.*, 2004] based on the clearly linear pattern of aftershocks in cross section and the coincidence between the predicted and observed surface fault dip for the upper segment. We see no evidence in the seismicity or InSAR data for significant synthetic faults at the eastern end of the rupture as suggested by *Meyer et al.* [1996] and *Rigo et al.* [2004].

[39] We have evaluated this fault interpretation using both nonlinear and linear inversion methods. Incorporation of this geometric model in linear slip inversions leads to a 32% improvement in the RMS residuals to surface deformation observed by InSAR when compared to an optimized planar fault model. The three-fault model incorporates the major observed surface rupture traces as well as honoring subsurface fault patterns imaged by high-precision aftershock locations. These independent data sets add further support for the three-fault model, although their contribution is difficult to quantify. Inclusion of additional fault segments imaged by the aftershocks does not significantly improve the fit to the observed surface deformation, suggesting that while these faults were clearly active during the seismic sequence they did not contribute significantly to the overall deformation.

[40] The best fitting model for the Kozani-Grevena event thus appears to be a three-segment rupture including a largely west striking segment dipping 43° north from 6 to 15 km depth, a steeper upper segment dipping 70° north from 0 to 6 km depth, and a segment striking 210° and dipping 65° at the southwestern end of the rupture. A broad area of high slip extends from 6 km depth near the east-west center of the fault to 15 km depth at the western end of the fault. This pattern is grossly similar to that estimated by *Rigo et al.* [2004]; however, the maximum value is greater (4.7 m versus 3.0 m) and located at the upper end of the area of high slip rather than at the lower end. Inclusion of a smoothing term within the slip inversion eliminates the high-frequency variability of slip seen in the Rigo model. The best fit double couple for the model has a similar strike and dip to previous geodetic and seismological estimates (Table 1); however, the seismic moment is about twice that of the seismological estimates and is closer to the geodetic estimate of *Clarke et al.* [1997] using GPS-triangulation data. The high slip values and high moment are a result of higher surface displacements (~63 cm) in our unwrapped interferogram than previously interpreted (~33 cm) [*Meyer et al.*, 1996; *Rigo et al.*, 2004].

[41] The Kozani-Grevena earthquake thus appears to have ruptured a largely blind moderately dipping normal fault and more steeply dipping linking structures, and this rupture apparently propagated onto a more steeply dipping

near-surface fault. The change in fault dip and the cut off in seismicity are located at the approximate depth of the base of the Mesohellenic basin. This fault model interpreted from the aftershock locations is consistent with the regional fault patterns. The main west striking fault segment is 28 km long; however, the main slip patch is limited to an area less than 20 km in length, similar to some of the longer fault segments in the region. The orientation of this fault is consistent with the major fault trends in the western part of the Aliakmon fault system. The more northerly trend of the southwestern segment of the main fault system is similar to other linking structures, both between the Serrvia and Deskati fault systems as well as within the Deskati fault system itself. Finally, the 70 degree dip of the upper fault segment that is not imaged by the aftershocks, but rather inferred from the surface ruptures and the top of seismicity is consistent with the fault dips observed at the surface for the Paleochori fault [*Meyer et al.*, 1996].

[42] The results of this study, including the interpreted fault patterns and coseismic slip distribution, have implications for our understanding of earthquake rupture on segmented faults and regional seismic hazard assessments. The rupture appears to have propagated across fault segments with strike and dip changes of approximately 25° and 30°, respectively. These results provide constraints on the use of segment length in estimating the maximum likely event for the region. The cluster of large aftershocks to the southwest images an unmapped fault on which slip was triggered by the Kozani-Grevena main shock. This fault has a minimum area of $\sim$28 km^2 and thus could generate a $M_w > 5.0$ event, representing an additional significant seismic hazard to the region.

6. Conclusions

[43] The integration of high-precision aftershock locations and modeling of surface deformation measured by satellite interferometry (InSAR) has helped us to create a more complete three-dimensional model of the Kozani-Grevena earthquake than either data set could provide on its own. High-precision aftershock locations provide detailed images of three-dimensional fault networks, but do not provide a means of evaluating the contribution of these faults to an earthquake. Inverse modeling of geodetic data provides a means for both evaluating the interpreted fault model in comparison to other proposed models and for modeling slip on the imaged fault. Using this approach, we have created a more complete kinematic model for the Kozani-Grevena earthquake that may form the basis of future seismic hazard assessments and investigations into earthquake mechanics.

[44] **Acknowledgments.** This research was funded in part by USGS National Earthquake Hazard Reduction Program external grant 02HQGR0050 to D. Pollard, the ARCO Stanford Graduate Fellowship to P. Resor, and the Stanford Rock Fracture Project. T. Wright is supported by a Royal Society University Research Fellowship. We wish to thank the P. Clarke, D. Hatzfeld, A. Kiratzi, B. Meyer, and G. Papadopolous, who willingly shared their data, as well as their many coworkers who collected and processed the seismological, geological, and geodetic data that helped make this project possible. Thanks to P. Cervelli and I. Koukouvelas, who provided constructive reviews which helped improve the final manuscript. Finally, thanks to E. Zanzerkia and F. Maerten for help with the Double Difference and Poly3dInv codes, respectively.

References

Armijo, R., et al. (1996), Quaternary evolution of the Corinth Rift and its implications for the late Cenozoic evolution of the Aegean, *Geophys. J. Int.*, *126*, 11–53.

Cervelli, P., et al. (2001), Estimating source parameters from deformation data, with an application to the March 1997 earthquake swarm off the Izu Peninsula, Japan, *J. Geophys. Res.*, *106*, 11,217–11,237.

Chiaraluce, L., W. L. Ellsworth, C. Chiarabba, and M. Cocco (2003), Imaging the complexity of an active normal fault system: The 1997 Colfiorito (central Italy) case study, *J. Geophys. Res.*, *108*(B6), 2294, doi:10.1029/2002JB002166.

Clarke, P. J., et al. (1997), Geodetic investigation of the May 13, 1995, Kozani-Grevena (Greece) earthquake, *Geophys. Res. Lett.*, *24*, 707–710.

Clarke, P. J., et al. (1998), Crustal strain in central Greece from repeated GPS measurements in the interval 1989–1997, *Geophys. J. Int.*, *135*, 195–214.

Comninou, M., and J. Dunders (1975), The angular dislocation in a half space, *J. Elast.*, *5*, 205–216.

Doutsos, T., and S. Kokkalas (2001), Stress and deformation patterns in the Aegean region, *J. Struct. Geol.*, *23*, 455–472.

Doutsos, T., and I. Koukouvelas (1998), Fractal analysis of normal faults in northwestern Aegean area, Greece, *J. Geodyn.*, *26*, 197–216.

Doutsos, T., et al. (1994), Intracontinental wedging and post-orogenic collapse in the Mesohellenic Trough, *Geol. Rundsc.*, *83*, 257–275.

Drakatos, G., et al. (1998), Observations on the 3-D crustal velocity structure in the Kozani-Grevena (NW Greece) area, *J. Geodyn.*, *26*, 341–351.

Du, Y., A. Aydin, and P. Segall (1992), Comparison of various inversion techniques as applied to the determination of a geophysical deformation model for the 1983 Borah Peak earthquake, *Bull. Seismol. Soc. Am.*, *82*, 1840–1866.

Dziewonski, A. M., et al. (1996), Centroid-moment tensor solutions for April-June 1995, *Phys. Earth Planet. Inter.*, *96*, 1–13.

Goldstein, R., and C. Werner (1998), Radar interferogram filtering for geophysical applications, *Geophys. Res. Lett.*, *25*, 4035–4038.

Goldsworthy, M., and J. Jackson (2000), Active normal fault evolution in Greece revealed by geomorphology and drainage patterns, *J. Geol. Soc.*, *157*, 967–981.

Goldsworthy, M., and J. Jackson (2001), Migration of activity within normal fault systems: Examples from the Quaternary of mainland Greece, *J. Struct. Geol.*, *23*, 489–506.

Goldsworthy, M., et al. (2002), The continuity of active fault systems in Greece, *Geophys. J. Int.*, *148*, 596–618.

Harris, R. A., and P. Segall (1987), Detection of a locked zone at depth on the Parkfield, California, segment of the San Andreas fault, *J. Geophys. Res.*, *92*, 7945–7962.

Hatzfeld, D., et al. (1995), The Kozani-Grevena (Greece) earthquake of May 13, 1995, M (sub S) = 6.6; preliminary results of a field multidisciplinary survey, *Seism. Res. Lett.*, *66*, 61–70.

Hatzfeld, D., et al. (1997), The Kozani-Grevena (Greece) earthquake of 13 May 1995 revised from a detailed seismological study, *Bull. Seismol. Soc. Am.*, *87*, 463–473.

Jackson, J. (1994), Active tectonics of the Aegean region, *Annu. Rev. Earth Planet. Sci.*, *22*, 239–271.

Jackson, J. A., and N. J. White (1989), Normal faulting in the upper continental-crust: Observations from regions of active extension, *J. Struct. Geol.*, *11*, 15–36.

Johnson, K., et al. (2001), Fault geometry and slip distribution of the 1999 Chi-Chi, Taiwan earthquake imaged from inversion of GPS data, *Geophys. Res. Lett.*, *28*, 2285–2288.

Jónsson, S., et al. (2002), Fault slip distribution of the 1999 M_w 7.1 Hector Mine, California, earthquake, estimated from satellite radar and GPS measurements, *Bull. Seismol. Soc. Am.*, *92*, 1377–1389.

Kilb, D., and A. M. Rubin (2002), Implications of diverse fault orientations imaged in relocated aftershocksof the Mount Lewis, M_L 5.7, California, earthquake, *J. Geophys. Res.*, *107*(B11), 2294, doi:10.1029/2001JB000149.

King, G. C. P. (1986), Speculations on the geometry of the initiation and termination process of earthquake rupture and its relation to morphology and geological structure, *Pure Appl. Geophys.*, *124*, 567–585.

Koukouvelas, I. K., and A. Aydin (2002), Fault structure and related basins of the North Aegean Sea and its surroundings, *Tectonics*, *21*(5), 1046, doi:10.1029/2001TC901037.

Lawson, C. L., and R. J. Hanson (1974), *Solving Least Squares Problems*, 340 pp., Prentice-Hall, Upper Saddle River, N. J.

Maerten, F., et al. (2005), Inverting for slip on three-dimensional fault surfaces using angular dislocations, *Bull. Seismol. Soc. Am.*, in press.

McClusky, S., et al. (2000), Global Positioning System constraints on plate kinematics and dynamics in the eastern Mediterranean and Caucasus, *J. Geophys. Res.*, *105*, 5695–5719.

McKenzie, D. P. (1970), Plate tectonics of the Mediterranean region, *Nature*, *226*, 239–243.

McKenzie, D. P. (1972), Active tectonics of the Mediterranean region, *Geophys. J. R. Astron. Soc.*, *30*, 109–185.

Meyer, B., et al. (1996), The 1995 Grevena (northern Greece) earthquake: Fault model constrained with tectonic observations and SAR interferometry, *Geophys. Res. Lett.*, *23*, 2677–2680.

Meyer, B., et al. (1998), Geodetic investigation of the May 13, 1995, Kozani-Grevena (Greece) earthquake discussion and reply, *Geophys. Res. Lett.*, *25*, 129–133.

Mountrakis, D., et al. (1998), Seismic fault geometry and kinematics of the 13 May 1995 western Macedonia (Greece) earthquake, *J. Geodyn.*, *26*, 175–196.

Mouyiaris, N., et al. (1989), Seismotectonic map of Greece with seismological data, Inst. Geol. and Miner. Explor., Athens, Greece.

Okada, Y. (1985), Surface deformation due to shear and tensile faults in a half-space, *Bull. Seismol. Soc. Am.*, *75*, 1,135–131,154.

Papazachos, B. C., et al. (1996), Focal properties of the 13 May 1995 large (M_s = 6.6) earthquake in the Kozani area (north Greece), in *Congress of the Carpatho - Balkan Geological Association, September 17–20, 1995, Athens, Greece*, *Spec. Publ. 6*, edited, pp. 96–106, Geol. Soc. of Greece, Athens.

Papazachos, B. C., B. G. Karakostas, A. A. Kiratzi, E. E. Papadimitriou, and C. B. Papazachos (1998), A model for the 1995 Kozani-Grevena seismic sequence, *J. Geodyn.*, *26*, 217–231.

Pavlides, S., and D. Mountrakis (1987), Extensional tectonics of northwestern Macedonia, Greece, since the late Miocene, *J. Struct. Geol.*, *9*, 385–392.

Pavlides, S. B., et al. (1995), The 13 May 1995 western Macedonia, Greece (Kozani Grevena) earthquake: Preliminary results, *Terra Nova*, *7*, 544–549.

Prejean, S., W. Ellsworth, M. Zoback, and F. Waldhauser (2002), Fault structure and kinematics of the Long Valley Caldera region, California, revealed by high-accuracy earthquake hypocenters and focal mechanism stress inversions, *J. Geophys. Res.*, *107*(B12), 2355, doi:10.1029/2001JB001168.

Rigo, A., et al. (2004), The 1995 Kozani-Grevena (northern Greece) earthquake revisited: An improved faulting model from synthetic aperture radar interferometry, *Geophys. J. Int.*, *157*, 727–736.

Roberts, S., and J. Jackson (1991), Active normal faulting in central Greece; an overview, Active normal faulting in central Greece: An overview, in *The Geometry of Normal Faults*, edited by A. M. Roberts, G. Yielding, and B. Freeman, *Geol. Soc. Spec. Publ.*, *56*, 125–142.

Rubin, A. M., et al. (1999), Streaks of microearthquakes along creeping faults, *Nature*, *400*, 635–641.

Schaff, D. P., G. H. R. Bokelmann, G. C. Beroza, F. Waldhauser, and W. L. Ellsworth (2002), High-resolution image of Calaveras Fault seismicity, *J. Geophys. Res.*, *107*(B9), 2186, doi:10.1029/2001JB000633.

Schwartz, D. P., and K. J. Coppersmith (1984), Fault behavior and characteristic earthquakes: Examples form the Wasatch and San Andreas Fault zones, *J. Geophys. Res.*, *89*, 5,681–685,698.

Segall, P., and D. D. Pollard (1987), Theoretical displacements and stresses near fractures in rock: With applications to faults, joints, veins, dikes and solution surfaces, in *Fracture Mechanics of Rock*, edited by B. K. Atkinson, pp. 277–349, Elsevier, New York.

Stein, R. S., and S. E. Barrientos (1985), Planar high-angle faulting in the Basin and Range; geodetic analysis of the 1983 Borah Peak, Idaho, earthquake, *J. Geophys. Res.*, *90*, 11,355–311,366.

Waldhauser, F., and W. L. Ellsworth (2000), A double-difference earthquake location algorithm: Method and application to the northern Hayward fault, California, *Bull. Seismol. Soc. Am.*, *90*, 1353–1368.

Welstead, S. (1999), *Fractal and Wavelet Image Compression Techniques*, 232 pp., SPIE Opt. Eng. Press, Bellingham, Wash.

Wernicke, B., et al. (1992), Cenozoic extensional tectonics of the U.S. Cordillera, in *The Geology of North America*, vol. G3, *The Cordilleran Orogen: Conterminous U. S.*, edited by B. C. Burchfiel et al., pp. 553–581, Geol. Soc. of Am., Boulder, Colo.

G. Beroza, Department of Geophysics, 397 Panama Mall, Stanford University, Stanford, CA 94305-2215, USA.

D. Pollard, Department of Geological and Environmental Sciences, 450 Serra Mall, Building 320, Stanford University, Stanford, CA 94305-2115, USA.

P. Resor, Department of Earth and Environmental Sciences, Wesleyan University, 265 Curch Street, Middletown, CT 064559, USA. (presor@wesleyan.edu)

T. Wright, COMET, Department of Earth Sciences, University of Oxford, Parks Road, Oxford OX1 3PR, UK.